Proceedings of the 17th Czech and Slovak Conference on Magnetism, Košice, Slovakia, June 3–7, 2019

Magnetic Phase Diagram of $Tm_{0.96}Yb_{0.04}B_{12}$ Antiferromagnet with Dynamic Charge Stripes and Yb Valence Instability

A. Azarevich[a,b,*], A. Bogach[a,c], S. Demishev[a,b], V. Glushkov[a,b], N. Shitsevalova[d], V. Filipov[d], S. Gabáni[e], G. Pristas[e], K. Flachbart[e], S. Gavrilkin[f] and N. Sluchanko[a,b]

[a]Prokhorov General Physics Institute, RAS, Vavilov str. 38, 119991 Moscow, Russia
[b]Moscow Institute of Physics and Technology, Institutskiy p.9, Dolgoprudny, Moscow Rg. 141700 Russia
[c]National University of Science and Technology "MISIS", Leninskiy pr.4, Moscow, 119049 Russia
[d]Institute for Problems of Materials Science, NASU, Krzhizhanovsky str., 3, 03142, Kyiv, Ukraine
[e]Institute of Experimental Physics SAS, Watsonova 47, 04001 Košice, Slovakia
[f]Lebedev Physical Institute of RAS, Leninskiy Prospekt 53, 119991 Moscow, Russia

Detailed studies of magnetoresistance, magnetization and heat capacity have been carried out at helium temperatures for single-domain crystals of antiferromagnetic (AF) metal $Tm_{0.96}Yb_{0.04}B_{12}$ with dynamic charge stripes and Yb valence instability. The results allowed us to construct the angular H–φ–T magnetic phase diagram in the form of a "Maltese cross". It was shown that the dramatic symmetry lowering in the AF ground state of this dodecaboride with fcc crystal structure could be attributed to the spin density redistribution of conduction electrons from the RKKY oscillations to dynamic charge stripes, which modify significantly the indirect exchange interaction between magnetic moments of Tm^{3+} ions, and result in appearance of a number of various magnetic phases and phase transitions. Doping with Yb strongly suppresses the AF long-range order which works upon the AF-paramagnet phase boundaries.

DOI: 10.12693/APhysPolA.137.788

PACS/topics: Maltese Cross anisotropy, Dynamic charge stripes

1. Introduction

Dynamics, or, fluctuating charge and spin stripes attract extraordinary scientific interest due to their possible role in high temperature superconductivity [1, 2]. Phase singularities accompanied by lowered lattice symmetry were detected in a number of cuprates including $La_{2-x}Ba_xCuO_4$ and $YBa_2Cu_3O_{7-\delta}$ [3, 4]. This kind of electronic instability is also suggested to be extremely important for an understanding of the physics of colossal magnetoresistive manganites, nickelates, iron-based superconductors [1–5], etc. Very recently, dynamic charge stripes have been detected in non-magnetic dodecaboride LuB_{12}, while their origin was explained in terms of the cooperative dynamic Jahn-Teller (JT) effect in boron B_{12} cubooctahedra, in which a kind of electron instability appears along the principal crystallographic direction [110] [6]. In [7], however, it has been discovered the formation of dynamic charge stripes within the semiconducting matrix of $Tm_{0.19}Yb_{0.81}B_{12}$. The charge dynamics in these conducting nanometer channels was characterized by broad-band optical spectroscopy that allowed estimating the frequency ($\sim 2.4\times10^{11}$ Hz) of quantum motion of the charge carriers. Moreover, because of Yb valence instability the direction of the nanosize filamentary structure becomes different from ⟨110⟩ [7]. Taking into account that $Tm_{1-x}Yb_xB_{12}$ with $x < 0.2$ are antiferromagnetic metals it looks promising to investigate the effect of the stripes on the magnetic phase diagram and charge carriers scattering in these strongly correlated electron systems. Therefore, in order to shed more light on the origin of both various regimes of carrier scattering and numerous magnetic phases in AF metals with dynamic charge stripes, we present here a detailed study of magnetoresistance $\Delta\rho/\rho$ in combination with heat capacity, and magnetization measurements of $Tm_{0.96}Yb_{0.04}B_{12}$.

2. Experimental details

The high quality single-domain crystals of $Tm_{0.96}Yb_{0.04}B_{12}$ ($T_N \approx 2.6$ K) were grown by vertical crucible-free inductive floating zone melting in an inert gas atmosphere. The quality of these crystals was controlled by X-ray diffraction, Laue backscattering-patterns, and electron microprobe analysis. Resistivity was measured by standard DC four-probe technique with the orientation of measuring current $\boldsymbol{I} \parallel [110]$. Magnetoresistance was studied at liquid helium temperatures 1.8–4.2 K in magnetic fields up to 80 kOe. In the experiment with sample rotation the direction of external magnetic field $\boldsymbol{H}$ was varied in the range of angles $\varphi = 0$–$90°$ (where $\varphi = \boldsymbol{H}\hat{\ }\boldsymbol{n}$, and $\boldsymbol{n} \parallel \langle 110\rangle$ is the normal vector to the sample surface). Heat capacity and magnetization measurements have been performed using PPMS and MPMS (Quantum Design).

*corresponding author; e-mail: azarevich@lt.gpi.ru

3. Results and discussion

Figure 1 shows the temperature dependencies of resistivity and heat capacity in zero field and magnetic susceptibility in low magnetic field ($H = 100$ Oe, $\boldsymbol{H} \parallel [100]$) of $\mathrm{Tm_{0.96}Yb_{0.04}B_{12}}$ antiferromagnetic metal with Néel temperature $T_\mathrm{N} \approx 2.6$ K in a wide temperature region including the antiferromagnet (AF) – paramagnet (P) phase transition. It is worth noting the sharp step-like anomaly of heat capacity and the resistivity kink which are accompanied by the presence of maximum of the susceptibility near T_N.

Figure 2a–c shows magnetic field dependencies of susceptibility $\mathrm{d}M/\mathrm{d}H = f(H)$ of $\mathrm{Tm_{0.96}Lu_{0.04}B_{12}}$ at various temperatures in the range 1.9–2.6 K, in magnetic fields up to 50 kOe aligned along three principal directions in the cubic lattice: $\boldsymbol{H} \parallel [100]$, $\boldsymbol{H} \parallel [011]$, and $\boldsymbol{H} \parallel [111]$.

As can be seen from Fig. 2a–c, additionally to the step-like anomaly near H_N (AF-P transition) the susceptibility shows several peaks at H_M (one for $\boldsymbol{H} \parallel [100]$ and $\boldsymbol{H} \parallel [111]$, and two for $\boldsymbol{H} \parallel [011]$) which correspond to orientation magnetic phase transitions inside the AF state. The results of magnetic measurements allow us to construct the magnetic phase diagrams for $\boldsymbol{H} \parallel [100]$, $\boldsymbol{H} \parallel [011]$ and $\boldsymbol{H} \parallel [111]$ (see Fig. 2d–f). It is easy to see that the AF-P phase boundary is strongly anisotropic. Indeed, the Néel field $H_\mathrm{N} \approx 39$–40 kOe detected at $T = 1.9$ K for $\boldsymbol{H} \parallel [011]$ and $\boldsymbol{H} \parallel [111]$ is essentially smaller than the value $H_\mathrm{N} \approx 48$ kOe observed in direction $\boldsymbol{H} \parallel [100]$ (Fig. 2d–f). On the contrary, the anisotropy found inside the AF state is quite different. The location of orientation phase transitions at H_M coincides for $\boldsymbol{H} \parallel [100]$ and $\boldsymbol{H} \parallel [111]$, but it differs strongly from these values for $\boldsymbol{H} \parallel [011]$, where two

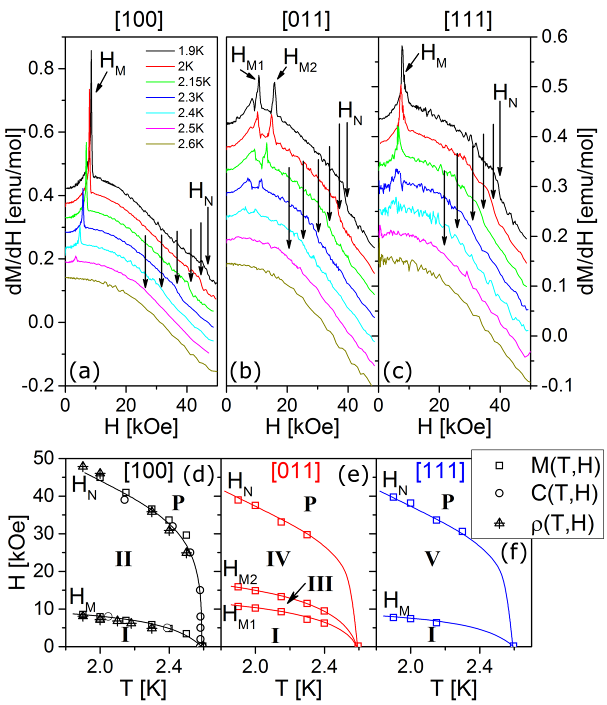

Fig. 2. (a)–(c) Field dependencies of magnetic susceptibility $\mathrm{d}M/\mathrm{d}H = f(H)$ of $\mathrm{Tm_{0.96}Yb_{0.04}B_{12}}$ at various temperatures in the range 1.9–2.6 K in magnetic fields up to 50 kOe for (a) $\boldsymbol{H} \parallel [100]$, (b) $\boldsymbol{H} \parallel [011]$, and (c) $\boldsymbol{H} \parallel [111]$. Arrows and symbols H_N and $H_{M1,2}$ indicate the magnetic phase transitions (see text). (d)–(f) H–T magnetic phase diagram of $\mathrm{Tm_{0.96}Yb_{0.04}B_{12}}$ for $\boldsymbol{H} \parallel [100]$, $\boldsymbol{H} \parallel [011]$ and $\boldsymbol{H} \parallel [111]$. The phase boundaries are derived from magnetoresistance, heat capacity, and magnetization data (see symbols for details). Roman numerals denote various phases within the AF state and P-paramagnetic phase.

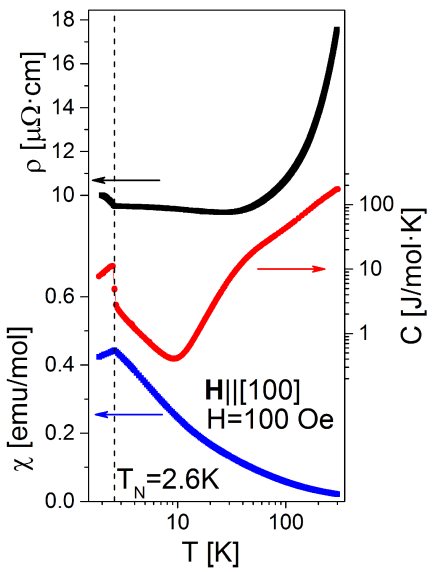

Fig. 1. Temperature dependencies of resistivity ($H = 0$), specific heat ($H = 0$), and susceptibility ($H = 100$ Oe, $\boldsymbol{H} \parallel [100]$) for $\mathrm{Tm_{0.96}Yb_{0.04}B_{12}}$.

phase transitions at H_{M1} and H_{M2} are observed and both of them are located at markedly higher magnetic fields (Fig. 2e). In order to construct the H–φ phase diagram at $T = 2$ K we have measured the magnetic field dependencies of magnetoresistance $\Delta\rho/\rho(H, \varphi_0)$ for several fixed φ_0 values in the range of angles $\varphi = 0$–$90°$ between $\boldsymbol{H} \parallel [100]$ ($\varphi_0 = 0$), and $\boldsymbol{H} \parallel [011]$ ($\varphi_0 = 90°$) (see Fig. 3).

It is seen in Fig. 3 that negative magnetoresistance dominates in $\mathrm{Tm_{0.96}Yb_{0.04}B_{12}}$ and the features on $\Delta\rho/\rho(H, \varphi_0)$ curves are observed for three principal directions at the same positions H_M and H_N, as it was detected in magnetic measurements (Fig. 2). Apart from $\boldsymbol{H} \parallel [100]$ direction, additional anomaly appears at H_{M3} slightly below H_N, and it shifts to low magnetic fields when φ increases in the range 0–37°. Moreover, in the sector $\varphi = 70$–$90°$ we indicate strong changes on $\Delta\rho/\rho(H, \varphi_0)$ curves which should be attributed to a dramatic variation of the phase boundaries in the AF state. Measurement in the full circle range $\varphi = 0$–$360°$ consistently reproduces data shown in Fig. 3. Figure 4 shows a color map polar plot of magnetoresistance and,

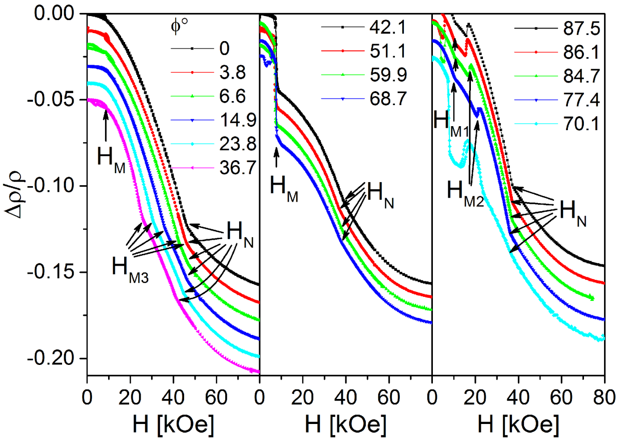

Fig. 3. Field dependencies of magnetoresistance at $T = 2$ K for various directions of magnetic field between $\boldsymbol{H} \parallel [100]$ ($\varphi_0 = 0$) and $\boldsymbol{H} \parallel [011]$ ($\varphi_0 = 90°$).

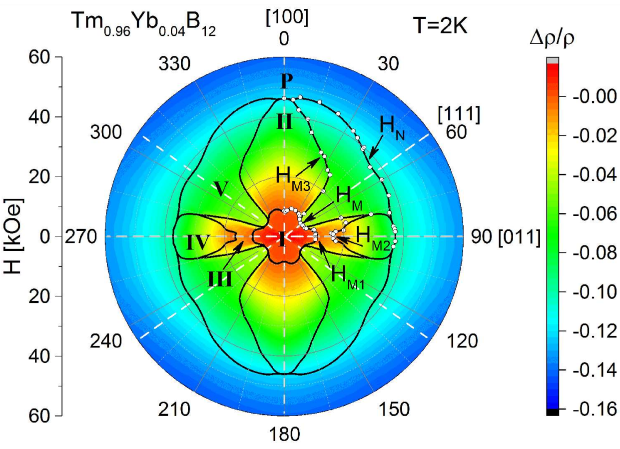

Fig. 4. Magnetoresistance field and angular dependencies at $T = 2$ K in the (1-10) plane (the rotation axis aligned along $\boldsymbol{I} \parallel [1\bar{1}0]$ is directed perpendicular). The phase boundaries of the H-φ magnetic phase diagram are derived from the magnetoresistance measurements. Roman numerals are the same as in Fig. 2 and denote various phases within the AF state.

simultaneously, H–φ phase diagram at $T = 2$ K in the (1-10) plane. It is easy to see that the transverse MR of the single-domain $Tm_{0.96}Yb_{0.04}B_{12}$ crystal with $\boldsymbol{I} \parallel [110]$ that this compound has in polar plots an anisotropic phase diagram in the form of a Maltese cross with lobes, which are arranged along ($\boldsymbol{H} \parallel [110]$) and transverse ($\boldsymbol{H} \parallel [001]$) to the dynamic charge stripes observed previously in $Tm_{1-x}Yb_xB_{12}$ [7]. At the same time both the strong anisotropy of AF–P phase boundary and essential changes in the shape of the lobes in comparison with $Ho_{0.8}Lu_{0.2}B_{12}$ [8] allow us to conclude about an essential role of Yb charge fluctuations (Yb valence ν(Yb)$\approx$ 2.95 [9]) on the depression of AF state in $Tm_{0.96}Yb_{0.04}B_{12}$.

4. Conclusions

A strongly correlated electron system $Tm_{0.96}Yb_{0.04}B_{12}$ with fcc lattice instability (cooperative dynamic JT effect), nanometer-size electronic phase separation (dynamic charge stripes) and Yb valence instability has been studied in detail by low temperature magnetoresistance, magnetization, and heat capacity measurements. An angular H–φ–T_0 antiferromagnetic phase diagram in the form of a Maltese cross has been deduced for this AF metal for the first time. We argue that the observed dramatic symmetry lowering is a consequence of strong renormalization of the indirect exchange interaction (RKKY mechanism) due to the presence of dynamic charge stripes in the matrix of AF metal. We propose also essential role of electron density fluctuations on Yb-sites on both the depression of AF state and changes in orientation of stripes in $Tm_{1-x}Yb_xB_{12}$ antiferromagnets, which are similar to those ones observed in the paramagnetic $Tm_{0.19}Yb_{0.81}B_{12}$ [7].

Acknowledgments

This work was supported by the Russian Science Foundation, project No. 17-12-01426 and Slovak agencies VEGA (grant No. 2/0032/16) and APVV (grant No. 17- 0020).

References

[1] M.R. Norman, D. Pines, C. Kallin, *Adv. Phys.* **54**, 715 (2005).

[2] M. Vojta, *Adv. Phys.* **58**, 699 (2009).

[3] J.M. Tranquada, B.J. Sternlieb, J.D. Axe, Y. Nakamura, S. Uchida, *Nature* **375**, 561 (1995).

[4] H.A. Mook, P. Dai, F. Dogan, R.D. Hunt, *Nature* **404**, 729 (2000).

[5] E. Dagotto, *Science* **309**, 257 (2005).

[6] N.B. Bolotina, A.P. Dudka, O.N. Khrykina, V.N. Krasnorussky, N.Yu. Shitsevalova, V.B. Filipov, N.E. Sluchanko, *J. Phys.: Condens. Matter* **30**, 265402 (2018).

[7] N.Sluchanko, A.N. Azarevich, A.V.Bogach et al., *J. Phys. Cond. Mat.* **31**, 065604 (2019).

[8] A.L. Khoroshilov, V.N. Krasnorussky, K.M. Krasikov et al., *Phys. Rev. B* **99**, 174430 (2019).

[9] T. Susaki, A. Sekiyama, K. Kobayashi et al., *Phys. Rev. Lett.* **77**, 4269 (1996).